IEEE/CSC SUPERCONDUCTIVITY NEWS FORUM (global edition) October 2014.
This ASC 2014 manuscript 2EPo2F-02 was published online in *IEEE Trans. Appl. Supercond.* *(IEEE XPLORE)* DOI:10/1109/TASC.2014.2372673, on November 20, 2014.

Towards the in-situ detection of individual He_2* excimers using a Ti TES in superfluid helium

Faustin W. Carter, Scott A. Hertel, Michael J. Rooks, Daniel N. McKinsey, and Daniel E. Prober

***Abstract*—We characterize a single titanium (Ti) transition edge sensor (TES) designed for in-situ detection of individual He_2* excimers. We find a critical temperature of 420 mK, an electrothermal time constant of $\sim$3 μs, and a total energy resolution of 1.5 eV. We observe the detector response to short laser pulses, and present a successful analysis strategy for extracting direct-TES-hit pulse areas from a much larger substrate hit background. We discuss near-term plans for coupling multiple such TESs together with a shared aluminum (Al) absorber, increasing the He_2* collection area to millimeter scales. Finally, we briefly discuss the technical challenges (and solutions) of installing a hermetic superfluid volume in a cryogen-free dilution refrigerator.**

***Index Terms*—Transition Edge Sensor, Helium excimer, UV Sensor**

I. Introduction

THE dynamics of quantum turbulence in superfluid ^{4}He is a field of active research. Quantum vortices are made observable by trapping particles within the vortex core. The particles used for tagging the vortices in this way would ideally be easily observed, long-lived, and small in diameter so as not to perturb the vortex dynamics under study. Micron-scale hydrogen ice particles have been used [1], [2], but He_2* excimers, produced in situ through electron bombardment [3], [4], [5] or laser ionization [6] offer significant advantages. Due to extremely weak spin-orbit coupling, this triplet He_2 ($a^3\Sigma_u^+$) state is metastable, with a lifetime of 13 s [7]. This state is 17.8 eV above ground, and releases photons spread in energy over a broad UV peak (13–18 eV) upon decay [8]. It releases a similar energy when non-radiatively quenched on a solid surface [9]. He_2* is efficiently and permanently trapped by quantum vortices (trapping radius $\sim$100 nm [11]). Although there are ongoing efforts to observe this trapped state using laser fluorescence [12], [13], to date this trapped state has been observed only through surface quenching [10], [11].

We aim to improve on the previous surface quenching observation studies through the use of a bolometric sensing technique. While the current-sensing apparatus of Zmeev et al [10], [11] is the state of the art and has produced significant new results, the charge-sensing technique suffers from low efficiency ($\leq 10^{-3}$) [14], and the resulting signals are, by necessity, averaged over many instances of quantum turbulence production spanning several days. Here, we describe progress towards measuring a He_2* flux using a TES sensor coupled to a large-area Al absorber, a technique which promises near unity intrinsic efficiency and should be capable of observing quantum turbulence dynamics on much shorter time scales.

The primary goal of this paper is to describe a preliminary characterization of the bare TES. We present the detector noise and signal response to a pulsed blue laser (470 nm) in vacuum, as well as a method for using the averaged noise over many traces to bootstrap a device characterization in the absence of a calibrated photon source. The second goal of this paper is to describe the experimental chamber and other necessary hardware in some detail. This necessary infrastructure has been built and successfully tested through several warming/cooling cycles in our cryostat. Here we provide some detail regarding construction methods (with commercial part numbers where available).

II. TES Detectors

A. Design

A well-designed TES is dominated by intrinsic thermal fluctuation noise, which is a strong function of the TES operating temperature T_c [15]. Some of the more common materials for TES fabrication are molybdenum/gold (Mo/Au) [16], titanium/gold (Ti/Au), and tungsten (W) [17]. We have decided for this demonstration project to employ a material that is well characterized in our laboratory, elemental titanium (Ti) [18], [19]. Although Ti has a critical temperature ($T_c \approx 350$ mK) that is somewhat higher than other options, its T_c is reproducible, avoiding the complexities of the variable (or, tunable) T_c values of Mo/Au, W, or Ti/Au. Our Ti TESs should still be sensitive to the 15 eV energy we expect from an excimer decay. Although our experiment requires a base temperature < 100 mK, a Ti TES with an Al absorber could also function in a pumped ^{3}He cryostat where the warmer base temperature means the Al will suffer less quasiparticle trapping (due to the Al gap variations) than below 100 mK [20], [21].

Thermal fluctuation noise in TESs is also a function of detector volume; TESs are typically made as small as possible (subject to retaining a linear response) in order to limit this noise [15]. To obtain a large signal collection area despite the sensor's small size, it is advantageous to employ an absorber that collects the photon or excimer energy and couples this energy into the TES. We are following a general approach currently in use by CDMS [22], and previously at Yale [23], [24], [25]. We employ an aluminum (Al) superconducting absorber. The absorbed energy breaks Cooper pairs in the Al, and the resulting quasiparticles diffuse within the Al and are

Manuscript received: Aug. 13, 2014
Facilities use was supported by YINQE and NSF MRSEC DMR-1119826. We also acknowledge support from the National Science Foundation under NSF DMR-1007974.
The authors are with Yale University, New Haven, CT 06511 USA (email: faustin.carter@yale.edu).

IEEE/CSC SUPERCONDUCTIVITY NEWS FORUM (global edition) October 2014.
This ASC 2014 manuscript 2EPo2F-02 was published online in *IEEE Trans. Appl. Supercond.* *(IEEE XPLORE)* DOI:10/1109/TASC.2014.2372673, on November 20, 2014.

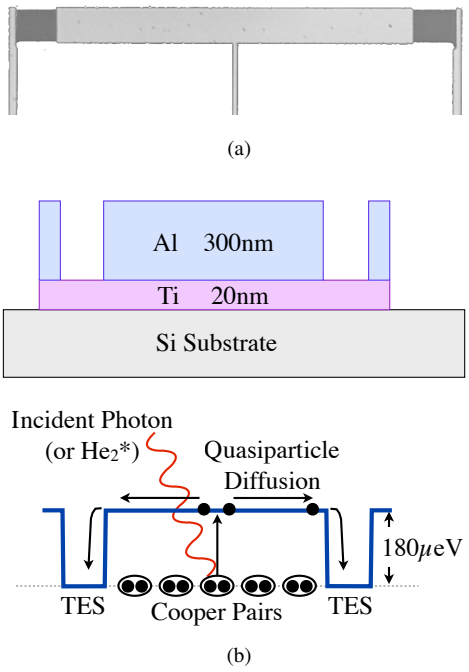

Fig. 1. (a) Optical microscope image (false color) showing an actual device. The Ti TESs are the grey squares and are 20x20 μm^2. (b)Top is a schematic of the detector cross section. Bottom is a depiction of the energy-level diagram showing the energy gap of the Al, and the lower-energy trapping regions of the Ti TESs, with nearly zero gap at their T_c.

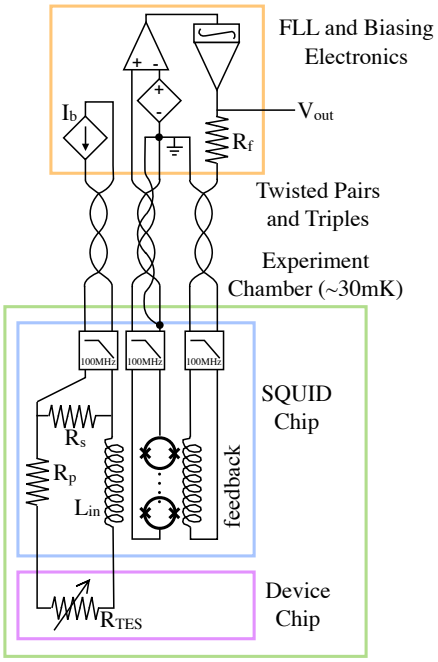

Fig. 2. The electrical readout scheme. The voltage across the feedback resistor is low-pass filtered at 1.9 MHz and read out by a digitizing oscilloscope.

eventually trapped by the TES [26]. This process is depicted in figure 1. In previous work we have measured the quasiparticle lifetime of our evaporated Al films to be quite long, allowing for a large (∼1 mm) absorber [27], [28]. If a single Al absorber is connected to multiple TESs, the position of the energy deposition in the absorber can be determined by comparing the relative pulse energies [24], [22], [29].

B. Fabrication

The present detectors are fabricated by evaporating a titanium/aluminum (Ti/Al) bilayer onto a high-resistivity silicon (Si) wafer through a poly-methyl-methacrylate (PMMA) lift-off mask defined by electron-beam lithography. The process has three steps; two lift-off steps, and one etch step. The final product is depicted in Fig. 1.

1. The Si wafer is first spun with PMMA and a pattern of alignment marks are written with the electron-beam lithography tool (a Raith EBPG). The alignment marks consist of 400 nm of copper (Cu) with a few nanometers of Ti underneath that serves as an adhesion layer. The unwanted metal is then lifted off by dissolving the PMMA mask in N-Methyl-2-pyrrolidone (NMP) that has been heated to 70 C.

2. The wafer is again spun with PMMA and the the detector-cum-absorber pattern is written via EBPG. A bilayer of 20 nm of Ti and 300 nm of Al is evaporated and then lifted off.

3. Another layer of PMMA is spun, and a window over the Ti TES region is opened via another EBPG write. The exposed Al is removed through a two-minute etch with tetramethyl ammonium hydroxide photoresist developer [30]; this completes the base detector.

Finally, the Si wafer is diced and the device is mounted to the experiment with a dab of GE Varnish [31] and wire-bonded to the board containing the SQUID Amplifiers.

C. Readout

We operate our TESs in the negative electrothermal feedback mode [32] and read them out with a commercial three-channel system. Each channel is read out using a single-stage SQUID amplifier and room-temperature flux locked loop (FLL) electronics [33], [34]. In this configuration the TES is in parallel with a small shunt resistor R_s and in series with an inductor $L = 5$ nH. The TES is voltage biased ($R_{TES} > R_s$). The inductor converts the current through the TES to a magnetic flux, which is then read out by the SQUID. Our output signal is the voltage across the feedback resistor R_f in the flux-locked loop. The circuit diagram is depicted in Fig. 2.

In any real implementation of this circuit, there is some parasitic lead resistance R_p between the TES and the inductor that couples to the SQUID. We have endeavored to use superconducting circuit board traces (tin-coated copper) where possible to minimize this resistance. In our configuration, $R_p = 5$ mΩ.

D. TES Characterization

Here we present the characterization of a single Ti TES with Al leads (and no Al absorber). The Ti TES is 40x40 μm^2 and is 20 nm thick. The device is pictured in the inset of Fig. 3. The Al leads are 300 nm thick, 5 μm wide and serve to contain the hot electrons within the TES so that the

IEEE/CSC SUPERCONDUCTIVITY NEWS FORUM (global edition) October 2014.
This ASC 2014 manuscript 2EPo2F-02 was published online in *IEEE Trans. Appl. Supercond.* *(IEEE XPLORE)* DOI:10/1109/TASC.2014.2372673, on November 20, 2014.

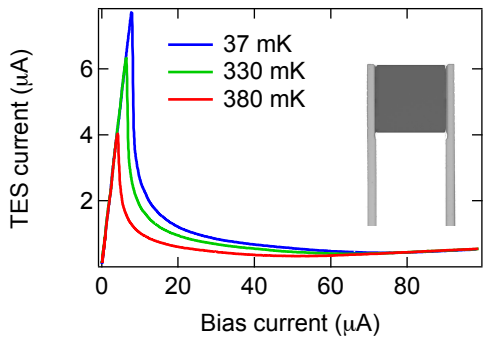

Fig. 3. Current through TES $I_{\rm TES}$ as a function of bias current $I_{\rm b}$. Inset shows optical microscope image of device. The dark area is the 20 nm thick Ti TES, which is 40x40 μm^2, and the lighter lengths are 300 nm thick Al leads.

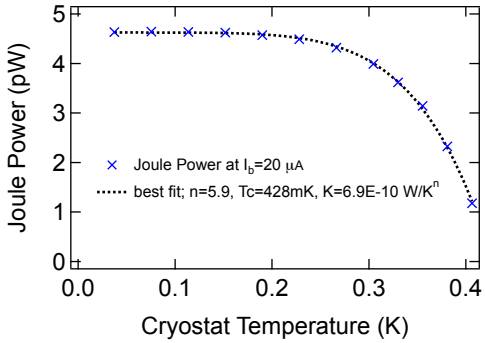

Fig. 4. Joule power dissipated by TES at constant bias current $I_{\rm b} = 20$ μA at different bath temperatures, fit using (2).

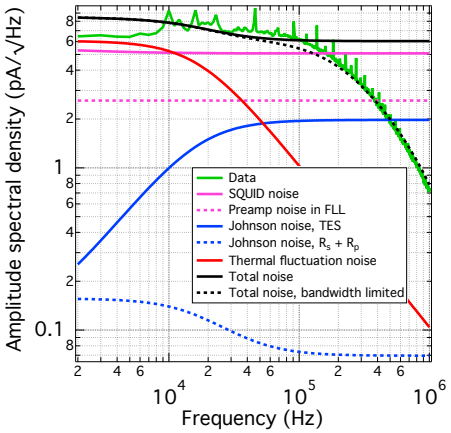

Fig. 5. Detector noise contributions referred to the TES current.

primary cooling channel is electron-phonon interaction within the TES rather than electron out-diffusion through the leads. The important quantities for predicting device performance are the heat capacity C, the thermal conductance G, the power-law exponent describing thermal conductance n (see (2)) the constant current logarithmic temperature sensitivity $\alpha_{\rm I}$, and the constant temperature logarithmic current sensitivity $\beta_{\rm I}$. Both $\alpha_{\rm I}$ and $\beta_{\rm I}$ are calculated using partial derivatives, and are related to the total alpha $\alpha_{\rm T}$ (the logarithmic sensitivity as a function of both current and temperature) through:

$$\alpha_{\rm T} = \frac{2\alpha_{\rm I} + \frac{n}{\phi}\beta_{\rm I}}{2\beta_{\rm I}} \qquad (1)$$

where $\phi = (1 - T_{\rm b}^n/T_{\rm c}^n)$ is a function of both $T_{\rm c}$ and the bath temperature $T_{\rm b}$. $\alpha_{\rm T}$ can be calculated from the curves in Fig. 3 and (2) [35].

Fig. 3 shows the current through the detector $I_{\rm TES}$ as a function of bias current $I_{\rm b}$ at different bath temperatures $T_{\rm b}$. The linear region at $I_{\rm b}$ is when the TES is fully superconducting, and the peak is when $I_{\rm b} = I_c$ where I_c is the critical current of the TES. A fit to this line gives a measurement of $R_{\rm p}$ provided $R_{\rm s}$ is known. The linear region at high $I_{\rm b}$ is when the TES is fully normal and a fit to this line gives the parallel combination of $R_{\rm s}$ and the TES normal resistance R_n. The smooth downward sloping curve in between the linear regions indicates bias currents for which the TES is biased within its superconducting transition.

Because it is not possible to measure $\alpha_{\rm I}$ directly when the TES is configured for electro-thermal feedback, it has been our practice to calculate $\alpha_{\rm T}$ from the $I_{\rm TES}$ vs $I_{\rm b}$ curve, relate $\beta_{\rm I}$ to $\alpha_{\rm I}$ through (1) and then fit the remaining parameter $\alpha_{\rm I}$ to the measured time constant τ of the TES. The model we use to do these fits is described in Irwin and Hilton [15].

We can calculate the resistance and Joule heating power $P_{\rm J}$ as a functions of $I_{\rm b}$. The optimal bias point for detection is when the power dissipation is flat as a function of $I_{\rm b}$. We have chosen to operate our device at $I_{\rm b} = 20$ μA, which gives us a device resistance $R_{\rm TES} = 3.9$ Ω.

The Joule power input to the TES is $P_{\rm J} = I_{\rm TES}^2 R_{\rm TES}$. In the flat region of the power curve, the TES is biased on its transition at its critical temperature $T_{\rm c}$ and is dissipating 100% of the Joule power via electron-phonon coupling. A power-law dependance for the electron-phonon mediated power loss is assumed and so

$$P_{\rm J} = I_{\rm TES}^2 R_{\rm TES} = K(T_{\rm c}^n - T_{\rm b}^n) \qquad (2)$$

where K is the electron-phonon coupling constant for the TES and n is an exponent that depends on the mechanism of power loss [15]. Most TESs have an n between 3–6. In order to determine the thermal conductivity of our TES at its bias point of 20 μA, we measure $P_{\rm J}$ vs $T_{\rm b}$ and fit it to (2) to determine K and n. The thermal conductivity G is then given by the $G = dP_{\rm J}/dT_{\rm b} = nKT_{\rm c}^{n-1}$. The data and the fit are shown in Fig. 4.

We have used these measured parameters to estimate the device noise, and compare it to actual noise measurements. Fig. 5 depicts the various theoretical contributions to the overall noise referred to the current through the TES as well as the actual measured current noise. The equations for the various noise contributions are found in Irwin and Hilton [15].

E. Device Response to Blue Laser Pulses

Here we present the response of the single pixel TES described in the previous section (see Fig. 3). Data from a two-TES device with an Al absorber will be presented in a future publication.

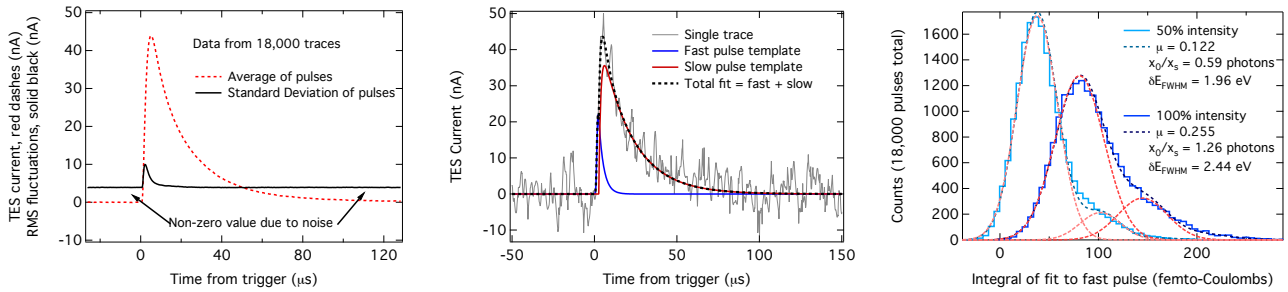

(a) (b) (c)

Fig. 6. (a) The average and standard deviation of 18 000 pulses at full intensity. (b) An example of the model used to fit the pulse data. (c) Histograms of integrals of the fast pulse fit. These histograms are fit by gaussian-broadened poisson distributions that have been scaled and shifted to fit the data according to 3. The dashed red curves show the first two terms ($n = 0, n = 1$) of each fit. One photon corresponds to roughly 64 fC.

The data presented in this section were taken by passing short pulses from a blue laser (470 nm, 2.6 eV) through a bank of adjustable neutral density filters, which couple into an optical fiber that terminates ∼1 cm above the TES. We triggered the oscilloscope on the laser pulse. We took pulse data at two attenuations that differed by a factor of two. We refer to these as 50% intensity and full intensity respectively. In each case, 18 000 pulses were recorded. Fig. 6a shows the average of 18 000 pulses and the standard deviation of pulses for the full intensity case. The average and standard deviation of the 50% attenuated pulses are characteristically similar, but roughly half as large in amplitude (the baseline of the standard deviation is the same for both attenuations).

At long time scales (> 10 μs), the pulses are well described by a falling exponential and are precisely repeatable, as can be seen in the standard deviation during this time, which is consistent with the pre-pulse noise. At short times (< 10 μs), the standard deviation reveals interesting variation between laser pulses, with a falling time constant suggestive of the calculated TES intrinsic fall time. Our interpretation is that the large, slow pulse is the result of energy delivered to the TES in the form of phonons, resulting from the large incident photon flux on the substrate. The faster, smaller component (the component which varies from pulse to pulse) is interpreted as arising from direct photon hits to the TES. The small, fast pulses are the more interesting component of the data, as they should obey Poisson statistics and can also be directly modeled by the equations in Irwin and Hilton [15].

We claim that the standard deviation can be used as a model pulse template for the fast component. To see this, let each pair of fast and slow pulses i be described by some amplitude A_i and function of time $f(t)$. Then $A_i^{\mathrm{f}} f^{\mathrm{f}}(t)$ and $A_i^{\mathrm{s}} f^{\mathrm{s}}(t)$ describe the fast and slow pulses respectively. The standard deviation of either pulse is then $\sigma(t) = \sigma_A f(t)$ where σ_A is the standard deviation of all A_i. If one assumes that the relative variation of the slow pulses is small ($\sigma^{\mathrm{s}}(t)/\overline{A^{\mathrm{s}}} \ll \sigma^{\mathrm{f}}(t)/\overline{A^{\mathrm{f}}}$), where $\overline{A}$ is the average pulse amplitude, then the standard deviation plotted in Fig. 6a is very nearly $\sigma^{\mathrm{total}}(t) = \sigma^{\mathrm{f}}(t) = \sigma_{\mathrm{A}}^{\mathrm{f}} f^{\mathrm{f}}(t)$, and is a good template for the fast pulse.

We used this template to extract the fast pulse component from each individual trace. We fixed the decay time, rise time, and temporal position of the template, while allowing the amplitude to vary. A slow pulse template was derived by fitting a combined (fast + slow) model to an average pulse, allowing all of the slow pulse parameters to be freely fit. Finally, the slow pulse template parameters were fixed, save for the amplitude, and the model (now with only two free parameters) was fit to all 18 000 traces. One of these fits is depicted in Fig. 6b. Histograms of the fitted fast pulse areas for both attenuations are shown in Fig. 6c.

The histograms were fit to the first five terms of a gaussian-broadened poisson distribution (3) where μ is average photon number, x_{s} is a scale factor that relates pulse integral to photon number, x_0 is an offset, and $\sigma_{\mathrm{s}} = x_{\mathrm{s}} * \delta E_{\mathrm{FWHM}}/(E_0 * 2\sqrt{2\ln 2})$ is related to the energy resolution δE of the detector as well as the deposited photon energy E_0. The initial guess for x_{s} was calculated by plugging all the measured device parameters into the Irwin and Hilton models, generating a model pulse for a single photon, and integrating the model. Likewise, the initial guess for σ_{s} was calculated from the Irwin and Hilton model. A is the area of the histogram being fit.

$$f(x) = A \sum_{n=1}^{5} \frac{e^{-\mu}\mu^n}{n} \frac{1}{2\sigma_{\mathrm{s}}} exp\left(-\frac{(x - x_0 - (nx_{\mathrm{s}}))^2}{2(\sigma_{\mathrm{s}})^2}\right) \quad (3)$$

We can calculate δE_{FWHM} from σ_{s}. For the full intensity histogram, $\sigma = \sigma_{\mathrm{s}}/x_{\mathrm{s}} = 0.39$ and $\delta E_{\mathrm{FWHM}} = 2.44$ eV. We can compare this to the intrinsic device resolution calculated from the Irwin and Hilton model, $\delta E_{\mathrm{FWHM}} = 0.6$ eV. The full system resolution is roughly four times worse than the theoretical value from the Irwin and Hilton model, but that is reasonable given that over much of our bandwidth we are dominated by amplifier and electronic noise (see Fig. 5) rather than intrinsic TES noise.

The fact that the histograms in Fig. 6c have both a width and an offset that is proportional to μ implies that there is some extra signal that is unaccounted for in our two-pulse model. We can estimate the best possible device energy resolution by extrapolating back and calculating $\delta E_{\mathrm{FWHM}} \approx 1.5$ eV at $\mu = 0$. We could achieve this best energy resolution by shielding the device from anything but a direct photon hit. Although this TES could not resolve single 470 nm photons even with such a shield, it should be able to resolve the 15 eV signal we expect to see from the He_2* excimers. Fig. 7

IEEE/CSC SUPERCONDUCTIVITY NEWS FORUM (global edition) October 2014.
This ASC 2014 manuscript 2EPo2F-02 was published online in *IEEE Trans. Appl. Supercond.* *(IEEE XPLORE)* DOI:10/1109/TASC.2014.2372673, on November 20, 2014.

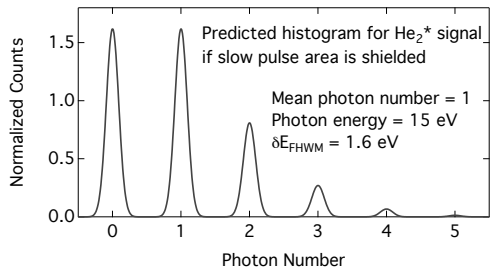

Fig. 7. Calculated TES response to hypothetical 15 eV excimer beam with $\mu = 1$ assuming half the energy couples into the TES.

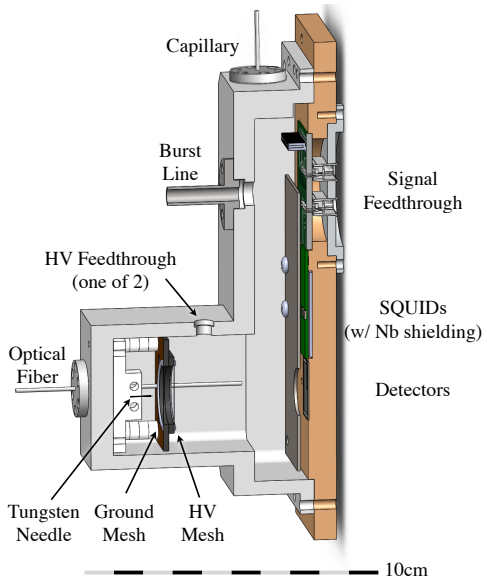

Fig. 8. Rendering of the experimental chamber. HV stands for high voltage (∼kV). The baseplate is manufactured from oxygen-free high thermal conductivity (OFHC) copper, the L-shaped top cap is machined from a single piece of aluminum, and the two are bolted together with an indium seal. The entire assembly is mounted in the depicted orientation on the cold plate of a dilution refrigerator.

shows a predicted histogram for photon emission by He_2* molecules with an average absorbed photon number $\mu = 1$. This calculation assumes that half of the photon energy will couple into the TES [36].

III. Experimental Chamber Design

The experimental chamber design posed several technical challenges, many the result of staging a complex process in a superfluid bath that tends to leak through even the smallest gaps. Fig. 8 shows a computer rendering of a cross-section of the experimental chamber. In this section we describe briefly the major components of the experiment as well as noting their functions.

A. Low Voltage

1) Low Voltage Wiring: Each of the three SQUID amplifier channels requires seven wires. In addition to these signal wires, we installed extra wiring for general use (thermometry level sensing, heaters, etc). Copper wire was used from room temperature to 4 K, and NbTi wire from 4 K to base. All 48 wires were assembled into two flat ribbon cables, which were heat sunk at each stage and fed into the superfluid volume through two micro-D hermetic flanges [37], which were laser welded into a circular flange and bolted to the chamber with an indium seal.

2) High Voltage: Although the ionization potential of He is quite high, it is possible to create He_2* through electron discharge from a sharp needle. To maximize electric field (or minimize the required voltage), we fabricated tungsten a needle with a $\approx$ 100 nm tip radius following a sodium-hydroxide etch recipe published by Golov and Ishimoto [38]. A slightly greater voltage is applied to a mesh that screens the tip to prevent the electrons from reaching our sensor plane.

To feed the two high-voltage (HV) lines into the chamber, we found that GPO-style thread-in hermetic feed-throughs [39] are both resilient at high voltage and are superfluid-tight when the supplied rubber O-ring is replaced with an indium seal. For the HV lines we used the same wire as in the low-voltage ribbon cables, with the addition of insulating teflon sleeves. We designed special heatsinking clamps for each stage, in which large surface areas counteracted the necessarily thick insulating layers.

B. Fiber Optics

We use a multi-mode fiber with a 300 μm diameter [40]. The fiber enters the cryostat through a hermetic seal at room temperature [41]. We have found that heat-sinking the fiber is unnecessary. The superfluid-tight feedthrough was created following the procedure of J.S. Butterworth et.al. [42], in which the seal is made through the thermal contraction of a length of heat-shrink tubing [43] during cool down.

C. Helium Plumbing

Helium is both injected and extracted using a thin stainless steel capillary. Our colleague A. Fragner [44] has found through trial and error that the optimal inner diameter is around 1 mm. He found that diameters below about 0.7 mm were prone to ice blockage, and that 1 mm is a good compromise between heat leak (through the superfluid Rollin film, $\propto r^2$) and fill time ($\propto r^4$). The capillary was heat-sunk at each stage by braising it into a spiral groove cut into OFHC copper posts. A. Fragner [44] also found that the swage-style connectors from HIP [45] can form superfluid-tight seals between two lengths of capillary tubing. To connect the capillary to the experimental chamber we use an indium-sealed flange brazed to the capillary.

To fill the chamber, we connect a helium volume of known volume and pressure to the capillary when the cryostat reaches 4 K, and that volume is cryo-pumped and eventually condensed into the chamber as the cryostat continues to cool to base (30 mK). To empty the chamber, we slowly apply heat and boil the liquid helium back into the storage vessel through the capillary. This fully-closed system is useful for two reasons: no liquid level measure is required, because a known quantity of gas entered the chamber, and no helium is lost (in the future we plan to use isotopically pure ^{4}He).

IEEE/CSC SUPERCONDUCTIVITY NEWS FORUM (global edition) October 2014.
This ASC 2014 manuscript 2EPo2F-02 was published online in *IEEE Trans. Appl. Supercond. (IEEE XPLORE)* DOI:10/1109/TASC.2014.2372673, on November 20, 2014.

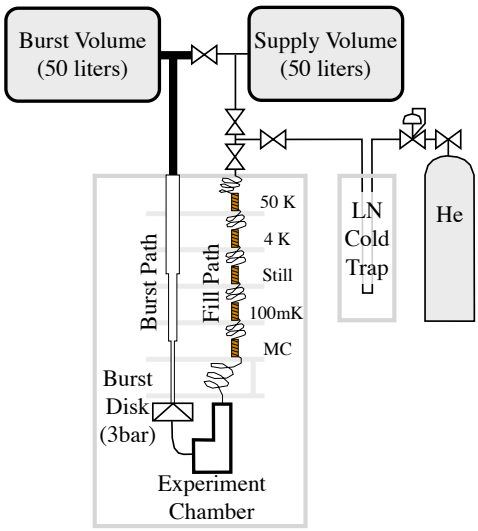

Fig. 9. Pumping circuit diagram depicting the He filling and safety lines. The mixing chamber (MC) stage typically reaches a temperature of 15 mK, while our experimental chamber which hangs off a mezzanine connected to the MC reaches a temperature of 30 mK.

In the event of a blockage in the capillary or a rapid warm-up event due to cryostat failure, the capillary may prove incapable of emptying the chamber fast enough to avoid dangerous pressures. To allow for the emergency decompression of the chamber, we have installed a large-diameter path from the chamber to an evacuated volume at room pressure. This emergency relief path is sealed from the chamber with a 3 bar burst-disk [46] at the cold stage. To accommodate the thermally expanding gas while minimizing the stainless steel thermal link, the burst line is constructed from a welded series of thin-walled tubes (10 mil) [47] of increasing diameter towards warmer stages to accommodate the gas expansion. Thermal baffles inside the burst line block blackbody radiation from the warmer stages.

The chamber was designed to minimize the amount of liquid helium, and thus the size of the room-temperature storage and burst volumes. Both the burst volume and the storage volume were off-the-shelf 50 L beer kegs [48], to which we welded KF-50 flanges [49]. Beer kegs are cheaper than any pressure vessel that is sold explicitly for scientific work and also ship food-grade clean. The entire helium plumbing system is depicted in Fig. 9

IV. Conclusions

1. A Ti TES should indeed be capable of resolving individual He_2* excimers. Despite the relatively high critical temperature of Ti, our analysis shows that this simple elemental TES ought to provide sufficient resolution to discriminate individual He_2 excimers (or any other quantized UV signal).

2. The two-pulse model works well for extracting TES hits from underneath substrate hits, and is a useful way to bootstrap a device calibration without a clearly visible photon peak separation, allowing us to use a convenient blue laser for calibration. Although our model still does not account for some of the input energy (see the histogram offsets in Fig. 6c) it is a useful approach for characterizing device parameters in the absence of either a calibrated deep UV photon source or an obvious Poisson distribution.

3. A smaller TES with a shield that eliminates photon absorption in the substrate will be better. In Fig. 5 the thermal fluctuation noise is slightly above the electronic noise at low frequencies. Making the TES smaller will bring this contribution down and then the signal will be truly amplifier-limited. Adding a shield will remove most (possibly all) of the large slow pulse. This will improve the resolution to at least 1.5 eV (see analysis at the end of section II-E). Since the offset suggests our fitting model is still not perfect, reducing the unwanted signal will likely further improve the resolution.

Acknowledgment

The authors would like to thank J. Cushman for drafting expertise; C. Matulis for circuit-board design; Dr. L. Frunzio for fabrication advice; Prof. R. Schoelkopf, Prof. M. Devoret, and Prof. M. Hatridge for cryogenics expertise; C. McKitterick, Dr. Z. Leghtas, and S. Touzard for helpful discussions; and the Gibbs Machine Shop for helping to make the experiment a reality.

References

[1] G. P. Bewley, D. P. Lathrop, and K. R. Sreenivasan, "Superfluid helium: visualization of quantized vortices." *Nature*, vol. 441, no. 7093, p. 588, Jun. 2006. [Online]. Available: http://www.ncbi.nlm.nih.gov/pubmed/16738652

[2] Y. A. Sergeev and C. F. Barenghi, "Particles-Vortex Interactions and Flow Visualization in ^{4}He," *J. Low Temp. Phys.*, vol. 157, no. 5-6, pp. 429–475, Oct. 2009. [Online]. Available: http://link.springer.com/10.1007/s10909-009-9994-8

[3] J. Keto, M. Stockton, and W. Fitzsimmons, "Dynamics of Atomic and Molecular Metastable States Produced in Electron-Bombarded Superfluid Helium," *Phys. Rev. Lett.*, vol. 28, no. 13, pp. 792–795, Mar. 1972. [Online]. Available: http://link.aps.org/doi/10.1103/PhysRevLett.28.792

[4] J. Keto, F. Soley, M. Stockton, and W. Fitzsimmons, "Dynamic properties of neutral excitations produced in electron-bombarded superfluid helium. I. The He(2 ^{3}S) and He_2 ($a^3\Sigma$) atomic and molecular metastable states," *Phys. Rev. A*, vol. 10, no. 3, pp. 872–886, Sep. 1974. [Online]. Available: http://link.aps.org/doi/10.1103/PhysRevA.10.872

[5] D. Tokaryk, R. Brooks, and J. Hunt, "Reaction dynamics of metastable helium molecules and atoms near 4.2 K," *Phys. Rev. A*, vol. 48, no. 1, pp. 364–381, Jul. 1993. [Online]. Available: http://link.aps.org/doi/10.1103/PhysRevA.48.364

[6] A. V. Benderskii, R. Zadoyan, N. Schwentner, and V. A. Apkarian, "Photodynamics in superfluid helium: Femtosecond laser-induced ionization, charge recombination, and preparation of molecular Rydberg states," *J. Chem. Phys.*, vol. 110, no. 3, p. 1542, 1999. [Online]. Available: http://scitation.aip.org/content/aip/journal/jcp/110/3/10.1063/1.477796

[7] D. McKinsey, C. Brome, J. Butterworth, S. Dzhosyuk, P. Huffman, C. Mattoni, J. Doyle, R. Golub, and K. Habicht, "Radiative decay of the metastable He_2 ($a^3\Sigma_u^+$) molecule in liquid helium," *Phys. Rev. A*, vol. 59, no. 1, pp. 200–204, Jan. 1999. [Online]. Available: http://link.aps.org/doi/10.1103/PhysRevA.59.200

[8] M. Stockton, J. Keto, and W. Fitzsimmons, "Ultraviolet Emission Spectrum of Electron-Bombarded Superfluid Helium," *Phys. Rev. Lett.*, vol. 24, no. 12, pp. 654–657, Mar. 1970. [Online]. Available: http://link.aps.org/doi/10.1103/PhysRevLett.24.654

[9] M. I. Trioni, G. Butti, N. Bonini, and G. P. Brivio, "Metastable helium spectroscopy on simple metals: Comparison between low and high work function substrates," *Surf. Sci.*, vol. 587, no. 1–2, pp. 121–127, Aug. 2005. [Online]. Available: http://linkinghub.elsevier.com/retrieve/pii/S0039602805004474

[10] D. E. Zmeev, F. Papkour, P. M. Walmsley, a. I. Golov, P. V. E. McClintock, S. N. Fisher, W. Guo, D. N. McKinsey, G. G. Ihas, and W. F. Vinen, "Observation of Crossover from Ballistic to Diffusion Regime for Excimer Molecules in Superfluid ^{4}He," *J. Low Temp. Phys.*, vol. 171, no. 3-4, pp. 207–213, Sep. 2012. [Online]. Available: http://link.springer.com/10.1007/s10909-012-0720-6

[11] D. E. Zmeev, F. Pakpour, P. M. Walmsley, a. I. Golov, W. Guo, D. N. McKinsey, G. G. Ihas, P. V. E. McClintock, S. N. Fisher, and W. F. Vinen, "Excimers He_2* as Tracers of Quantum Turbulence in ^{4}He in the $T = 0$ Limit," *Phys. Rev. Lett.*, vol. 110, no. 17, p. 175303, Apr. 2013. [Online]. Available: http://link.aps.org/doi/10.1103/PhysRevLett.110.175303

[12] W. Rellergert, S. Cahn, A. Garvan, J. Hanson, W. Lippincott, J. Nikkel, and D. McKinsey, "Detection and Imaging of He_2 Molecules in Superfluid Helium," *Phys. Rev. Lett.*, vol. 100, no. 2, p. 025301, Jan. 2008. [Online]. Available: http://link.aps.org/doi/10.1103/PhysRevLett.100.025301

[13] D. McKinsey, W. Lippincott, J. Nikkel, and W. Rellergert, "Trace Detection of Metastable Helium Molecules in Superfluid Helium by Laser-Induced Fluorescence," *Phys. Rev. Lett.*, vol. 95, no. 11, p. 111101, Sep. 2005. [Online]. Available: http://link.aps.org/doi/10.1103/PhysRevLett.95.111101

[14] R. Mehrotra, E. K. Mann, and A. J. Dahm, "A Study of the Neutral Excitation Current in Liquid ^{4}He above 1K," *J. Low Temp. Phys.*, vol. 36, no. 1-2, pp. 47–65, Dec. 1978. [Online]. Available: http://http://link.springer.com/article/10.1007/%2FBF00174911

[15] K. Irwin and G. Hilton, "Transition-edge sensors," in *Cryog. Part. Detect.*, C. Enss, Ed. Springer Berlin Heidelberg, 2005, vol. 99, pp. 63–150. [Online]. Available: http://link.springer.com/chapter/10.1007/10933596_3

[16] T. C. Chen, F. M. Finkbeiner, A. Bier, and B. DiCamillo, "Molybdenum-gold proximity bilayers as transition edge sensors for microcalorimeters and bolometers," *Supercond. Sci. Technol.*, vol. 12, no. 11, pp. 840–842, Nov. 1999. [Online]. Available: http://iopscience.iop.org/0953-2048/12/11/344

[17] a.E. Lita, D. Rosenberg, S. Nam, A. Miller, D. Balzar, L. Kaatz, and R. Schwall, "Tuning of Tungsten Thin Film Superconducting Transition Temperature for Fabrication of Photon Number Resolving Detectors," *IEEE Trans. Appiled Supercond.*, vol. 15, no. 2, pp. 3528–3531, Jun. 2005. [Online]. Available: http://ieeexplore.ieee.org/lpdocs/epic03/wrapper.htm?arnumber=1440433

[18] D. F. Santavicca, B. Reulet, B. S. Karasik, S. V. Pereverzev, D. Olaya, M. E. Gershenson, L. Frunzio, D. E. Prober, B. Young, B. Cabrera, and A. Miller, "Characterization of Terahertz Single-Photon-Sensitive Bolometric Detectors Using a Pulsed Microwave Technique," in *Aip Conf. ...*, 2009, pp. 72–75. [Online]. Available: http://scitation.aip.org/content/aip/proceeding/aipcp/10.1063/1.3292445

[19] D. F. Santavicca, B. Reulet, B. S. Karasik, S. V. Pereverzev, D. Olaya, M. E. Gershenson, L. Frunzio, and D. E. Prober, "Energy resolution of terahertz single-photon-sensitive bolometric detectors," *Appl. Phys. Lett.*, vol. 96, no. 8, p. 083505, 2010. [Online]. Available: http://scitation.aip.org/content/aip/journal/apl/96/8/10.1063/1.3336008

[20] B. Cabrera, Private Communication, May 2014.

[21] K. Segall, "Noise and Quasiparticle Dynamics in Single Photon, Superconducting Tunnel Junction Detectors," Ph.D. dissertation, Yale University, 2000. [Online]. Available: http://www.yale.edu/proberlab/Papers/SegallDissertation.pdf

[22] M. Pyle, P. Brink, B. Cabrera, J. Castle, P. Colling, C. Chang, J. Cooley, T. Lipus, R. Ogburn, and B. Young, "Quasiparticle propagation in aluminum fins and tungsten TES dynamics in the CDMS ZIP detector," *Nucl. Instruments Methods Phys. Res. Sect. A Accel. Spectrometers, Detect. Assoc. Equip.*, vol. 559, no. 2, pp. 405–407, Apr. 2006. [Online]. Available: http://linkinghub.elsevier.com/retrieve/pii/S0168900205024137

[23] L. Li, L. Frunzio, C. Wilson, and D. Prober, "Physical properties of the superconducting Ta film absorber of an X-ray photon detector," *IEEE Trans. Appiled Supercond.*, vol. 13, no. 2, pp. 1124–1127, Jun. 2003. [Online]. Available: http://ieeexplore.ieee.org/lpdocs/epic03/wrapper.htm?arnumber=1211804

[24] L. Li, L. Frunzio, C. M. Wilson, and D. E. Prober, "Quasiparticle nonequilibrium dynamics in a superconducting Ta film," *J. Appl. Phys.*, vol. 93, no. 2, p. 1137, 2003. [Online]. Available: http://scitation.aip.org/content/aip/journal/jap/93/2/10.1063/1.1533106

[25] L. Li, "X-ray single photon imaging detectors using superconducting tunnel junctions," Ph.D. dissertation, Yale University, 2003. [Online]. Available: http://www.yale.edu/proberlab/Papers/LiDissertation.pdf

[26] K. D. Irwin, S. W. Nam, B. Cabrera, B. Chugg, and B. a. Young, "A quasiparticle-trap-assisted transition-edge sensor for phonon-mediated particle detection," *Rev. Sci. Instrum.*, vol. 66, no. 11, p. 5322, 1995. [Online]. Available: http://scitation.aip.org/content/aip/journal/rsi/66/11/10.1063/1.1146105

[27] C. Wilson, L. Frunzio, and D. Prober, "Time-Resolved Measurements of Thermodynamic Fluctuations of the Particle Number in a Nondegenerate Fermi Gas," *Phys. Rev. Lett.*, vol. 87, no. 6, p. 067004, Jul. 2001. [Online]. Available: http://link.aps.org/doi/10.1103/PhysRevLett.87.067004

[28] C. Wilson and D. Prober, "Quasiparticle number fluctuations in superconductors," *Phys. Rev. B*, vol. 69, no. 9, p. 094524, Mar. 2004. [Online]. Available: http://link.aps.org/doi/10.1103/PhysRevB.69.094524

[29] E. Figueroa-Feliciano, "POSITION-SENSITIVE QUANTUM CALORIMETERS," Ph.D. dissertation, Stanford University, 2001.

[30] Dow Chemical, part number Microposit MF-312 Developer, http://dow.com.

[31] LakeShore Cryotronics, part number VGE-7031, http://www.lakeshore.com/.

[32] K. D. Irwin, "An application of electrothermal feedback for high resolution cryogenic particle detection," *Appl. Phys. Lett.*, vol. 66, no. 15, p. 1998, 1995. [Online]. Available: http://scitation.aip.org/content/aip/journal/apl/66/15/10.1063/1.113674

[33] Magnicon, XXF-1 SQUID Readout Electronics, http://www.magnicon.com.

[34] D. Drung, C. Assmann, J. Beyer, A. Kirste, M. Peters, F. Ruede, and T. Schurig, "Highly Sensitive and Easy-to-Use SQUID Sensors," *IEEE Trans. Appl. Supercond.*, vol. 17, no. 2, pp. 699–704, Jun. 2007. [Online]. Available: http://ieeexplore.ieee.org/lpdocs/epic03/wrapper.htm?arnumber=4277368

[35] K. Kinnunen, "Studies of transition-edge sensor physics: thermal models and noise," Ph.D. dissertation, University of Jyväskylä, 2011. [Online]. Available: https://jyx.jyu.fi/dspace/handle/123456789/37197

[36] P. Brink, "Non-equilibrium superconductivity induced by x-ray photons," Ph.D. dissertation, Oxford University, 1995.

[37] SRI Hermetics Inc., Part number SRIMD505-25-B, http://www.srihermetics.com. The Ceramax proprietary ceramic forms a superfluid-tight seal between each beryllium-copper pin and the surrounding stainless steel body.

[38] A. Golov and H. Ishimoto, "Sharp and stable metal tips for helium ionization at mK temperatures," *J. low Temp. Phys.*, vol. 113, pp. 957–962, 1998. [Online]. Available: http://link.springer.com/article/10.1023/A:1022583729253

[39] Corning Gilbert, part number 0119-783-1, http://corning.com.

[40] ThorLabs, part number FT300UMT, http://www.thorlabs.com/.

[41] Ocean Optics, part number VFT-400-UV-16, http://www.oceanoptics.com/.

[42] J. S. Butterworth, C. R. Brome, P. R. Huffman, C. E. H. Mattoni, D. N. McKinsey, and J. M. Doyle, "A demountable cryogenic feedthrough for plastic optical fibers," *Rev. Sci. Instrum.*, vol. 69, no. 10, p. 3697, 1998. [Online]. Available: http://scitation.aip.org/content/aip/journal/rsi/69/10/10.1063/1.1149161

[43] TE Connectivity, part number MFT-MT1000-NO.2-X-SP, http://www.te.com/. We tried several brands and types of heat shrink tubing. The part listed above is the only one that tested superfluid-leak-tight.

[44] A. Fragner, "Circuit Quantum Electrodynamics with Electrons on Helium," Ph.D. dissertation, Yale University, 2013. [Online]. Available: http://gradworks.umi.com/35/78/3578340.html

[45] High Pressure Equipment Company, part number 15-21AF1, http://www.highpressure.com.

[46] Oseco, http://www.oseco.com/.

[47] Vita Needle Company, http://vitaneedle.com.

[48] Kegco, part number KC HS-K15.5G-DDI, http://kegco.com.

[49] Kurt J. Lesker Company, part number QF50-224-SS, http://lesker.com.